

New Angles on Energy Correlators

Samuel Alipour-fard,^{1,*} Ankita Budhraj,^{2,†} Jesse Thaler,^{1,‡} and Wouter J. Waalewijn^{2,3,§}

¹*Center for Theoretical Physics, Massachusetts Institute of Technology, Cambridge, MA 02139, USA*

²*Nikhef, Theory Group, Science Park 105, 1098 XG, Amsterdam, The Netherlands*

³*Institute for Theoretical Physics Amsterdam and Delta Institute for Theoretical Physics, University of Amsterdam, Science Park 904, 1098 XH Amsterdam, The Netherlands*

Energy correlators have recently come to the forefront of jet substructure studies at colliders due to their remarkable properties: they naturally separate physics at different scales, are robust to contamination from soft radiation, and offer a direct connection with quantum field theory. The current parametrization used for energy correlators, however, is based on redundant pairwise angles with complex phase space restrictions. In this Letter, we introduce a new parametrization of energy correlators that features a simpler phase space structure and preserves information about the orientation of jet constituents. Further, our parametrization drastically reduces the computational cost to compute energy correlators on experimental data; whereas the time to compute a traditional projected N -point energy correlator scales as $M^N/N!$ on a jet with M particles, our new parametrization achieves a scaling of $M^2 \ln M$ independently of N . Theoretical calculations for our new energy correlators differ from those of traditional parametrizations only at next-to-next-to-leading logarithmic accuracy and beyond, and we expect that our simpler phase space structure will simplify those calculations. We also discuss how to extend our parametrization to resolved N -point energy correlators that encode angular distances between greater numbers of particles, and we propose two possible generalizations for probing multi-prong jets and testing jet scaling behaviour.

Introduction — The flow of energy within hadronic jets is an indispensable probe of Quantum Chromodynamics (QCD) [1–6]. Energy correlator observables [7–11] are particularly powerful tools for understanding energy flow both theoretically and experimentally [12–14]. Since energy correlators can be described directly in terms of field-theoretic energy flow operators [15–22], one can use sophisticated theoretical techniques, including the powerful technology of conformal field theories [19, 23], to extract rich information about jet substructure, especially in the collinear limit [24–37].

Recent work has highlighted the role of N -point energy correlators (ENCs) in precisely understanding the fundamental structure of particle interactions. ENCs probe angular correlations between N final-state particles, which offers a simple and intuitive way to separate physics at different scales and mitigate contamination from soft radiation. Applications focused on the Large Hadron Collider (LHC) include the top quark mass [38–40], hadronization transition [41, 42], dead-cone effect [43], gluon saturation [44], medium modifications in heavy-ion collisions [45–51], and predictions for the energy flow of charged particles [52–55]. Further, energy correlators have yielded the most precise jet substructure measurement of the strong coupling constant to date [13].

In this Letter, we introduce a new parametrization for energy correlators with a number of improved properties. First, our parametrization of the projected N -point energy correlator (PENC) depends on the largest distance R_1 to a “special” particle s in a set of N particles, suitably averaged over all choices for s ; this yields simpler phase space restrictions than the traditional parametrization for the PENC in terms of the largest pairwise angle [25]. Second, when considering more differential information, our parametrization of re-

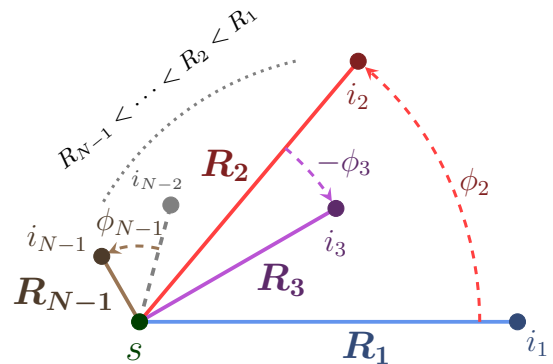


FIG. 1. A cartoon of the new parametrization of ENCs we introduce in Eqs. (2) and (5). Instead of computing the ENC using all $\binom{N}{2}$ pairwise distances, we parametrize the ENC with $2N - 3$ oriented polar coordinates centered on a special particle s , and then perform a momentum-weighted sum over all choices for s .

solved ENCs (RENC) employs non-redundant polar coordinates centered around the special particle, as in Fig. 1; this differs from the traditional approach, which uses over-complete information from the set of all pairwise distances and neglects information about the relative orientation of particles. Third, our parametrization offers dramatic improvements in computational performance. Finally, we anticipate that these conceptual and computational improvements will yield simpler theoretical calculations. The implementation of the PENCs we introduce in this work can be found on GitHub as an update to FASTEEC [56], and of our PENCs and RENCs at ResolvedEnergyCorrelators [57].

Review of Energy Correlators — In proton-proton collisions – the focus of this Letter – PENCs are usually defined via [25]:

$$\frac{1}{\sigma} \frac{d\sigma_N}{dR_L} = \left\langle \sum_{i_1 \dots i_N} z_{i_1} z_{i_2} \dots z_{i_N} \delta(R_L - \max_{k,\ell} \{R_{i_k, i_\ell}\}) \right\rangle. \quad (1)$$

Here, $z_i = p_{T,i}/\sum_j p_{T,j}$ is the transverse momentum fraction carried by particle i in the jet, $R_{i_k, i_\ell} = \sqrt{(y_{i_k, i_\ell})^2 + (\phi_{i_k, i_\ell})^2}$ is the angular separation between particles i_k and i_ℓ in the rapidity-azimuth plane, and the angular brackets indicate an expectation value over a sample of many hadronic jets. The sum over $\{i_k\}_{k=1}^N$ indicates the sum over all sets of N particles of a jet, and the variable R_L characterizes the maximum pairwise angular separation between the i_k .

However, the expression of Eq. (1) is computationally expensive due to the intricate phase space constraint $R_L = \max_{k,\ell} \{R_{i_k, i_\ell}\}$. For example, the time required to compute the (integer) PENC scales as $M^N/N!$ for a jet with M particles; when analytically continued to non-integer values of N , the PENC suffers a computational scaling of 2^{2M} .¹ This computational cost impedes several exciting PENC applications. For example, PENCs have an approximate scaling behavior related to the N -th Mellin moment of the DGLAP splitting functions [25]; the analytic continuation of the PENC to non-integer N therefore provides access both to the full splitting functions of QCD and, in the limit $N \rightarrow 0$, a unique opportunity to study small- x physics and BFKL dynamics with jets [25, 36, 58]. At very large values of N , PENCs also encode additional fundamental features of QCD [25, 59], such as level crossings with twist-4 operators. Furthermore, in the high-multiplicity environment of heavy ion collisions, even computing PENCs for $N = 3$ has been computationally challenging, limiting their potential in studying medium effects [51]. Improved computational efficiency is therefore necessary to leverage the full potential of PENCs in the study of realistic data samples.

Higher-point ENCs also yield more detailed shape information about the structure of radiation inside jets. For example, recent work has leveraged the E3C to propose a new method for extracting the top quark mass from experimental data [38–40]. Notably, for $N > 3$ the parametrization of ENCs in terms of the R_{i_k, i_ℓ} is over-complete: the R_{i_k, i_ℓ} describe $\binom{N}{2}$ distances, while only $2N - 3$ are independent.

New Angles: the Projected Case — In this Letter, we introduce a new parametrization of PENCs with a sim-

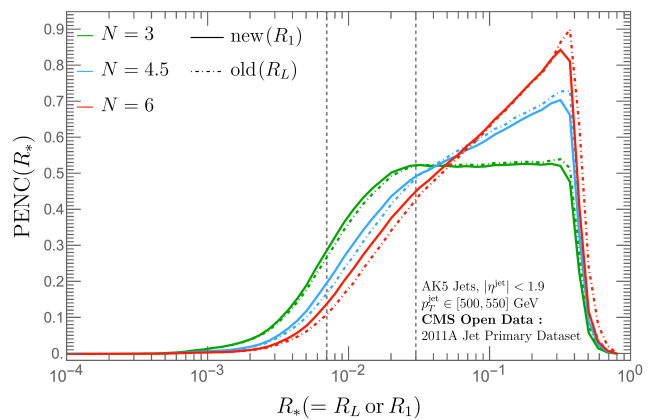


FIG. 2. PENC distributions for $N = \{3, 4.5, 6\}$, calculated using our new parametrization (solid) and the traditional parametrization (dashed). R_* denotes the largest distance to the special particle for our new parametrization (R_1), and the largest separation between the N particles for the traditional one (R_L). The differences are small in the perturbative region $R_* \gg \Lambda_{\text{QCD}}/p_T$, but become noticeable in the transition between perturbative and non-perturbative regimes (indicated by the vertical dashed lines).

pler phase space structure:

$$\begin{aligned} \frac{1}{\sigma} \frac{d\sigma_N}{dR_1} &= \left\langle \sum_{s=1}^M z_s \sum_{i_1 \dots i_{N-1}} z_{i_1} \dots z_{i_{N-1}} \delta(R_1 - \max_j \{R_{s, i_j}\}) \right\rangle, \\ &\equiv \text{PENC}(R_1). \end{aligned} \quad (2)$$

The sums on s and $\{i_j\}_{j=1}^{N-1}$ again run over all M particles within a jet. The crucial simplification is that our PENC is based on a new variable, R_1 , that indicates the maximum distance $\max\{R_{s, i_j}\}$ between the *single* particle s and any of the remaining $N - 1$ particles $\{i_j\}_{j=1}^{N-1}$.

Like the old variable R_L of Eq. (1), R_1 still roughly characterizes the maximum angular scale between a set of N particles, since $R_L/2 \leq R_1 \leq R_L$ by the triangle inequality. Indeed, the PENCs displayed in Fig. 2 show that the difference between our parametrization and that of Eq. (1) is small, and that both parametrizations have similar scaling behavior in the perturbative region (though there are some differences in the perturbative to non-perturbative transition). Figs. 2, 3, and 4 all feature energy correlators evaluated on the CMS 2011A Jet Primary Dataset [60, 61], also available in MIT Open Data format [62, 63], on jets with transverse momenta $p_T^{\text{jet}} \in [500, 550]$ GeV and pseudo-rapidity $|\eta^{\text{jet}}| < 1.9$.

Improved Computation Time — The computational efficiency of our parametrization is more evident in the (normalized) cumulative distribution:

$$\Sigma_N(R_1) = \frac{1}{\sigma} \int_0^{R_1} dR'_1 \frac{d\sigma_N}{dR'_1} = \left\langle \sum_s z_s [z_{\text{disk}}(s, R_1)]^{N-1} \right\rangle, \quad (3)$$

¹ FASTEEC [35] achieves a substantial speed up by replacing particles with subjects whose radius is chosen dynamically, depending on the desired level of angular resolution. For non-integer N , FASTEEC furthermore uses a recursive algorithm that reduces the standard 2^{2M} scaling down to $M 2^M$ [36].

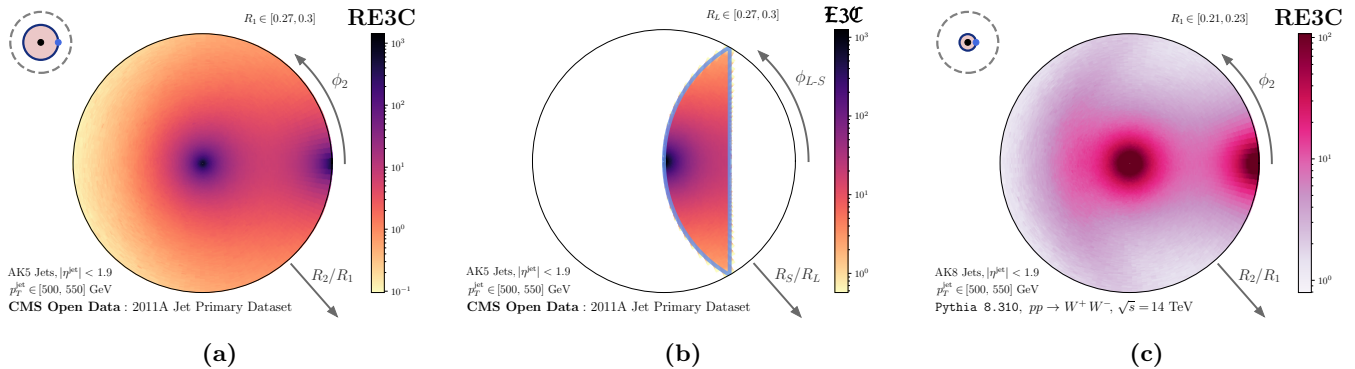


FIG. 3. Polar heat maps visualizing **(a)** our new RE3C applied to CMS Open Data, **(b)** the traditional E3C applied to CMS Open Data, and **(c)** our new parametrization applied to W -boson-initiated jets from `Pythia 8.310`. In **(a)** and **(c)**, the radial variables correspond to R_2/R_1 , the polar angle corresponds to ϕ_2 , and we show the RE3C in the bin $R_1 \in [0.27, 0.3]$. In **(b)** the radius corresponds to R_S/R_L , the polar angle corresponds to the angle between associated lines of length R_S and R_L , and we show the E3C in the bin $R_L \in [0.27, 0.3]$. In all three plots, we see collinear enhancements for the RE3C near the origin, when two particles become very close in angle. In **(a)** and **(c)**, we also see collinear enhancements as $R_2/R_1 \rightarrow 1$ and $\phi_2 \rightarrow 0$, and **(c)** exhibits additional non-collinear enhancements correlated with the W -boson mass.

where $z_{\text{disk}}(s, R_1)$ denotes the total transverse momentum fraction of all particles within a radius R_1 of the special particle s . Notably, the simple form of Eq. (3) holds even for non-integer N . A practical way to evaluate Eq. (3) (and Eq. (2) after differentiation) is, for each s , to first sort all particles by their distance with respect to s , and then to compute $\Sigma_N(R_1)$ by beginning with $R_1 = 0$ and then increasing it. Sorting particles by their distance to s takes $M \ln M$ time, and the remaining sum over s scales with M , resulting in an overall computation time scaling as $M^2 \ln M$. This computational speed up is especially interesting for heavy-ion collisions where M is typically very large.

Theoretical Perspectives — The factorization formula for the traditional PENCs [25] also applies to our new PENCs, with one small difference: because the variables R_1 and R_L differ for three or more emissions, the jet function for our PENCs differs from the old one at $\mathcal{O}(\alpha_s^2)$, or at next-to-next-to-leading logarithmic accuracy (NNLL). In the supplemental material, we discuss how the NLL equivalence of jet functions implies that $\Sigma_N(R_L) = \Sigma_N(R_1 = R_L[1 + \mathcal{O}(\alpha_s)])$. Furthermore, at NNLL and beyond, we expect that the simple dependence of Eq. (3) on N will substantially simplify the calculation of the jet function for R_1 . By contrast, the jet function using the old parametrization requires dedicated calculations for each individual value of N [24, 31].

Finally, we note that Eq. (3) is the N -th Mellin moment in z of

$$\frac{1}{\sigma} \frac{d\sigma}{dz}(R_1) = \left\langle \sum_s z_s \delta[z - z_{\text{disk}}(s, R_1)] \right\rangle, \quad (4)$$

which is also the differential jet rate in a jets-without-jets approach if R_1 is treated as a jet radius [64, 65]. A similar moment relation between the jet rate and the original ENC was noted in Ref. [66].

New Angles: the General Case — By including (or *resolving*) more detailed angular information about the positions and relative orientations of particles within the jet, we may generalize our new parametrization for the PENC to introduce the RENC:

$$\begin{aligned} \text{RENC}(R_1, R_2, \phi_2, R_3, \phi_3, \dots) &\equiv \frac{1}{\sigma} \frac{d\sigma_N}{dR_1 dR_2 d\phi_2 dR_3 d\phi_3 \dots} \\ &= \left\langle \sum_s z_s \sum_{i_1 \geq \dots \geq i_{N-1}} z_{i_1} \dots z_{i_{N-1}} \binom{N}{n_1 n_2 \dots} \delta(R_1 - R_{s, i_1}) \right. \\ &\quad \left. \times \rho_{i_2}(R_2, \phi_2) \rho_{i_3}(R_3, \phi_3) \dots \right\rangle, \quad (5) \end{aligned}$$

where for each s , the i_j are indexed such that $R_{s, i_1} \geq R_{s, i_2} \geq \dots$, and the summand involves the per-particle densities:

$$\rho_{i_j}(R_j, \phi_j) = \delta(R_j - R_{s, i_j}) \delta(\phi_j - \phi_{i_{j-1}, i_j}). \quad (6)$$

The “...” correspond to additional R_j and ϕ_j , and n_k denotes how often particle k of the jet appears among the i_j (such that terms with $n_k > 1$ encode self-correlations of particle k), with $\sum_{k=1}^M n_k = N$.

Our parametrization is visualized in Fig. 1, and utilizes polar coordinates around s , ordered in radius $R_1 > R_2 > \dots$ and with an *oriented* azimuthal angle ϕ_j taken relative to the $(j-1)$ -th resolved emission. The R_j and ϕ_j use $2N - 3$ variables to completely characterize the positions of all particles in the jet, relative to the axis defined by particles s and i_1 . The multinomial coefficient in Eq. (5) arises due to the ordering of the R_j , and accounts for the possibility that two or more of the i_j may be equal. Integrating inclusively over $\{R_j, \phi_j\}_{j=2}^N$ (which sets the third line of Eq. (5) to unity) reduces the RENC to the PENC from Eq. (2).

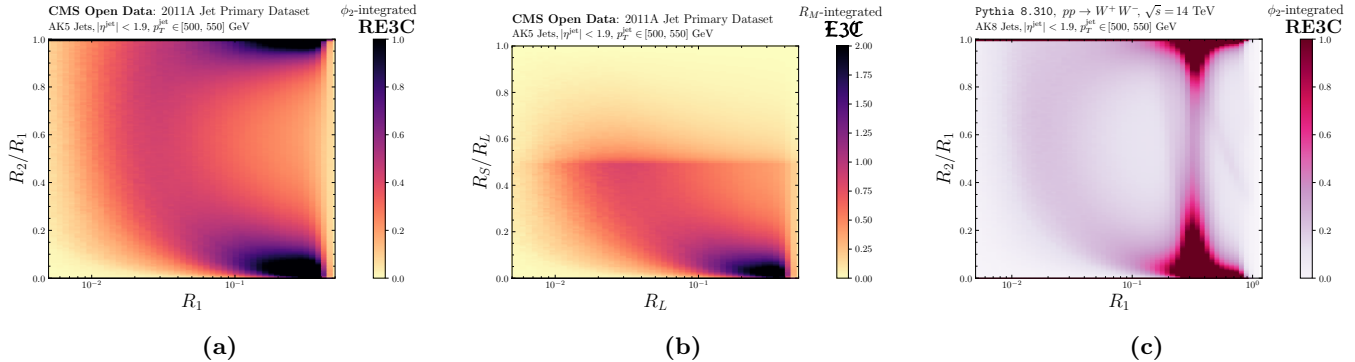


FIG. 4. Normalized distributions (a) our new RE3C applied to CMS Open Data when integrated over the azimuthal angle ϕ_2 , (b) the traditional E3C applied to CMS Open Data integrated over the intermediate angle R_M (analogous to integrating over ϕ_s), and (c) our new, ϕ_2 -integrated RE3C applied to W -boson-initiated jets.

The RENCs we introduce also preserve information about relative orientations, whereas even in the simple example of $N = 3$, the traditional E3C parametrization in terms of the largest (R_L), medium (R_M), and shortest (R_S) distances does not. We visualize the additional orientation information preserved by our RE3Cs in Figs. 3(a) and 3(b), where we compare polar heat maps of our parametrization of the RE3C to the traditional parametrization of the E3C. The additional angular information carried by our new RE3C also leads to striking visual differences when comparing jets initiated by different processes. For example, the unique characteristics of the RE3C evaluated on W -boson initiated jets generated with *Pythia* 8.310, shown in Fig. 3(c), clearly distinguish it from the RE3C of QCD-initiated jets. We provide similar visualizations for additional processes in the supplemental material.

The squeezed limit of our new RE3C, $R_2 \ll R_1$, is quite similar to the squeezed limit of the traditional E3C, $R_S \ll R_L$; in this limit, $R_2 \sim R_S$ and $R_1 \sim R_L$. Our new RE3C and the traditional E3C evaluated on CMS Open Data are compared in Figs. 4(a) and 4(b), which demonstrate that they indeed take similar forms when $R_S/R_L, R_2/R_1 < \frac{1}{2}$. When $R_S/R_L > \frac{1}{2}$, however, the traditional E3C is suppressed due to the hierarchy $R_S < R_M < R_L$. In Fig. 4(c), we visualize our new RE3C on *Pythia*-generated W jets, which exhibits a non-perturbative ridge similar to the one seen in CMS Open Data as well as additional features at $R_1 = 0.3$ correlated with the W mass, $R_1 \sim 2m_W/p_T$. In the supplemental material, we explain the ridge-like features in these plots from the perspective of non-perturbative physics.

Finally, we note that each additional resolved particle (i.e. each (R_j, ϕ_j) pair) introduces a factor of M to the scaling of the RENC computation time. In contrast, the computation time for e.g. the traditional 4-point correlator scales as M^4 independent of how many angles were resolved.

Generalizations — For completeness, we mention two

additional generalizations of our new parametrization for energy correlators – RENCs with two special particles and RENCs with two projected angles – for which we defer more detailed explorations to future work. For the energy correlator with two special particles,

$$\frac{1}{\sigma} \frac{d\sigma_{N,N'}}{dR dR_1 dR'_1} = \left\langle \sum_s z_s \sum_{s'} z_{s'} \delta(R - R_{ss'}) \right. \quad (7)$$

$$\times \sum_{i_1 \dots i_{N-1}} z_{i_1} \dots z_{i_{N-1}} \delta(R_1 - \max\{R_{s,i_k}\})$$

$$\left. \times \sum_{j_1 \dots j_{N'-1}} z_{j_1} \dots z_{j_{N'-1}} \delta(R'_1 - \max\{R_{s',j_k}\}) \right\rangle,$$

the two special particles s and s' are separated by a distance R , and R_1 and R'_1 denote the maximum distance of other particles to s and s' , respectively. This parametrization may capture interesting features of the radiation patterns of intrinsically 2-prong jets, e.g. from the hadronic decays of W or Higgs bosons, with a straightforward extension to three or more special particles for higher-prong jets.

We also define a *double*-projected energy-correlator,

$$\frac{1}{\sigma} \frac{d\sigma_{(a,b)}}{dR_1 dR_2} = \left\langle \sum_s z_s \sum_{i_1 \dots i_a} z_{i_1} \dots z_{i_a} \delta(R_1 - \max\{R_{s,i_k}\}) \right. \quad (8)$$

$$\left. \times \sum_{j_1 \dots j_b} z_{j_1} \dots z_{j_b} \delta(R_2 - \max\{R_{s,j_k}\}) \right\rangle,$$

where we again take $R_1 > R_2$. The associated cumulative distribution, analogous to Eq. (3), is

$$\Sigma_{(a,b)}(R_1, R_2) = \frac{1}{\sigma} \int_0^{R_1} dR'_1 \int_0^{R_2} dR'_2 \frac{d\sigma_{a,b}}{dR'_1 dR'_2}$$

$$= \left\langle \sum_s z_s [z_{\text{disk}}(s, R_1)]^a [z_{\text{disk}}(s, R_2)]^b \right\rangle, \quad (9)$$

highlighting that there is no additional complication when a, b are non-integer. Because the effective scaling

of this observable is set by $N = 1 + a + b$ and because the $N = 1$ moment of the DGLAP splitting functions vanish, we expect very mild dependence on R_1 at fixed R_2/R_1 when $b = -a$. This behavior therefore offers an interesting test of parton shower generators.

Discussion and Outlook — Motivated by the tremendous success and potential of energy correlators, this Letter introduces a new parametrization for higher-point correlators with several distinct advantages for both theoretical and data-driven analyses. Our new parametrization exhibits dramatically improved computational efficiency when evaluated on experimental data (without approximations), preserves information about the parity and relative orientation between particles within jets, and has intuitive features that benefit data visualization. We also expect that the simplified phase space will streamline theoretical calculations, the inclusion of hadronization effects, and pile-up subtraction. Additionally, our parametrization does not involve any re-

dundancy of phase space variables, unlike traditional parametrizations. We anticipate that the reparametrization of energy correlators we introduce in this work will benefit current studies of energy flow within hadronic jets and open new avenues for the use of energy correlators in the study of particle collisions.

Acknowledgements — We thank Kyle Lee, Ian Moult, and Aditya Pathak for inspiring discussions. J.T. thanks Arjun Kudinoor, Yen-Jie Lee, and Krishna Rajagopal for conversations about computational and visualization challenges with the traditional ENC parametrization. A.B. is supported by the project “Microscopy of the Quark Gluon Plasma using high-energy probes” (project number VI.C.182.054) which is partly financed by the Dutch Research Council (NWO). S.A.F. and J.T. are supported by the U.S. DOE Office of High Energy Physics under grant number DE-SC0012567. J.T. is additionally supported by the Simons Foundation through Investigator grant 929241. W.W. would like to thank the MIT CTP for hospitality, where this work was initiated.

-
- * samuelaf@mit.edu
† abudhraj@nikhef.nl
‡ jthaler@mit.edu
§ w.j.waalewijn@uva.nl
- [1] James D. Bjorken and Stanley J. Brodsky, “Statistical model for electron-positron annihilation into hadrons,” *Phys. Rev. D* **1**, 1416–1420 (1970).
 - [2] Howard Georgi and Marie Machacek, “Simple quantum-chromodynamics prediction of jet structure in e^+e^- annihilation,” *Phys. Rev. Lett.* **39**, 1237–1239 (1977).
 - [3] Edward Farhi, “Quantum chromodynamics test for jets,” *Phys. Rev. Lett.* **39**, 1587–1588 (1977).
 - [4] G. Parisi, “Superinclusive cross sections,” *Physics Letters B* **74**, 65–67 (1978).
 - [5] John F. Donoghue, F. E. Low, and So-Young Pi, “Tensor analysis of hadronic jets in quantum chromodynamics,” *Phys. Rev. D* **20**, 2759–2762 (1979).
 - [6] P.E.L. Rakow and B.R. Webber, “Transverse momentum moments of hadron distributions in qcd jets,” *Nuclear Physics B* **191**, 63–74 (1981).
 - [7] George F. Sterman, “Jet Structure in e^+e^- Annihilation with Massless Hadrons,” (1975).
 - [8] C. Louis Basham, Lowell S. Brown, S. D. Ellis, and S. T. Love, “Electron - Positron Annihilation Energy Pattern in Quantum Chromodynamics: Asymptotically Free Perturbation Theory,” *Phys. Rev. D* **17**, 2298 (1978).
 - [9] C.Louis Basham, Lowell S. Brown, Stephen D. Ellis, and Sherwin T. Love, “Energy Correlations in electron - Positron Annihilation: Testing QCD,” *Phys. Rev. Lett.* **41**, 1585 (1978).
 - [10] C.L. Basham, L.S. Brown, S.D. Ellis, and S.T. Love, “Energy Correlations in electron-Positron Annihilation in Quantum Chromodynamics: Asymptotically Free Perturbation Theory,” *Phys. Rev. D* **19**, 2018 (1979).
 - [11] C. Louis Basham, Lowell S. Brown, Stephen D. Ellis, and Sherwin T. Love, “Energy Correlations in Perturbative Quantum Chromodynamics: A Conjecture for All Orders,” *Phys. Lett. B* **85**, 297–299 (1979).
 - [12] Marianna Mazzilli (ALICE), “Measurements of HF-tagged jet substructure and energy-energy correlators with ALICE,” *PoS EPS-HEP2023*, 262 (2024).
 - [13] Aram Hayrapetyan *et al.* (CMS), “Measurement of energy correlators inside jets and determination of the strong coupling $\alpha_S(m_Z)$,” (2024), arXiv:2402.13864 [hep-ex].
 - [14] Andrew Tamis (STAR), “Measurement of Two-Point Energy Correlators Within1 Jets in $p p$ Collisions at $\sqrt{s} = 200$ GeV at STAR,” *PoS HardProbes2023*, 175 (2024), arXiv:2309.05761 [hep-ex].
 - [15] N.A. Sveshnikov and F.V. Tkachov, “Jets and quantum field theory,” *Phys. Lett. B* **382**, 403–408 (1996), arXiv:hep-ph/9512370.
 - [16] Fyodor V. Tkachov, “Measuring multi - jet structure of hadronic energy flow or What is a jet?” *Int. J. Mod. Phys. A* **12**, 5411–5529 (1997), arXiv:hep-ph/9601308.
 - [17] Gregory P. Korchemsky and George F. Sterman, “Power corrections to event shapes and factorization,” *Nucl. Phys. B* **555**, 335–351 (1999), arXiv:hep-ph/9902341.
 - [18] Christopher Lee and George F. Sterman, “Momentum Flow Correlations from Event Shapes: Factorized Soft Gluons and Soft-Collinear Effective Theory,” *Phys. Rev. D* **75**, 014022 (2007), arXiv:hep-ph/0611061.
 - [19] Diego M. Hofman and Juan Maldacena, “Conformal collider physics: Energy and charge correlations,” *JHEP* **05**, 012 (2008), arXiv:0803.1467 [hep-th].
 - [20] A.V. Belitsky, S. Hohenegger, G.P. Korchemsky, E. Sokatchev, and A. Zhiboedov, “From correlation functions to event shapes,” *Nucl. Phys. B* **884**, 305–343 (2014), arXiv:1309.0769 [hep-th].
 - [21] A.V. Belitsky, S. Hohenegger, G.P. Korchemsky, E. Sokatchev, and A. Zhiboedov, “Event shapes in $\mathcal{N} = 4$ super-Yang-Mills theory,” *Nucl. Phys. B* **884**, 206–256 (2014), arXiv:1309.1424 [hep-th].
 - [22] Petr Kravchuk and David Simmons-Duffin, “Light-ray operators in conformal field theory,” *JHEP* **11**, 102 (2018), arXiv:1805.00098 [hep-th].

- [23] Murat Kologlu, Petr Kravchuk, David Simmons-Duffin, and Alexander Zhiboedov, “The light-ray OPE and conformal colliders,” *JHEP* **01**, 128 (2021), arXiv:1905.01311 [hep-th].
- [24] Lance J. Dixon, Ian Moulton, and Hua Xing Zhu, “Collinear limit of the energy-energy correlator,” *Phys. Rev. D* **100**, 014009 (2019), arXiv:1905.01310 [hep-ph].
- [25] Hao Chen, Ian Moulton, Xiaoyuan Zhang, and Hua Xing Zhu, “Rethinking jets with energy correlators: Tracks, resummation, and analytic continuation,” *Phys. Rev. D* **102**, 054012 (2020), arXiv:2004.11381 [hep-ph].
- [26] Hao Chen, Ming-Xing Luo, Ian Moulton, Tong-Zhi Yang, Xiaoyuan Zhang, and Hua Xing Zhu, “Three point energy correlators in the collinear limit: symmetries, dualities and analytic results,” *JHEP* **08**, 028 (2020), arXiv:1912.11050 [hep-ph].
- [27] Hao Chen, Ian Moulton, and Hua Xing Zhu, “Quantum Interference in Jet Substructure from Spinning Gluons,” *Phys. Rev. Lett.* **126**, 112003 (2021), arXiv:2011.02492 [hep-ph].
- [28] Hao Chen, Ian Moulton, and Hua Xing Zhu, “Spinning gluons from the QCD light-ray OPE,” *JHEP* **08**, 233 (2022), arXiv:2104.00009 [hep-ph].
- [29] Stella T. Schindler, Iain W. Stewart, and Zhiqian Sun, “Renormalons in the energy-energy correlator,” (2023), arXiv:2305.19311 [hep-ph].
- [30] Anjie Gao, Hai Tao Li, Ian Moulton, and Hua Xing Zhu, “The Transverse Energy-Energy Correlator at Next-to-Next-to-Next-to-Leading Logarithm,” (2023), arXiv:2312.16408 [hep-ph].
- [31] Wen Chen, Jun Gao, Yibei Li, Zhen Xu, Xiaoyuan Zhang, and Hua Xing Zhu, “NNLL Resummation for Projected Three-Point Energy Correlator,” (2023), arXiv:2307.07510 [hep-ph].
- [32] Dmitry Chicherin, Ian Moulton, Emery Sokatchev, Kai Yan, and Yunyue Zhu, “The Collinear Limit of the Four-Point Energy Correlator in $\mathcal{N} = 4$ Super Yang-Mills Theory,” (2024), arXiv:2401.06463 [hep-th].
- [33] Hao Chen, Pier Francesco Monni, Zhen Xu, and Hua Xing Zhu, “Scaling violation in power corrections to energy correlators from the light-ray OPE,” (2024), arXiv:2406.06668 [hep-ph].
- [34] Cyuan-Han Chang and David Simmons-Duffin, “Three-point energy correlators and the celestial block expansion,” (2022), arXiv:2202.04090 [hep-th].
- [35] Ankita Budhraj and Wouter J. Waalewijn, “FastEEC: Fast Evaluation of N-point Energy Correlators,” (2024), arXiv:2406.08577 [hep-ph].
- [36] Ankita Budhraj, Hao Chen, and Wouter J. Waalewijn, “ ν -point energy correlators with FastEEC: small- x physics from LHC jets,” (2024), arXiv:2409.12235 [hep-ph].
- [37] Kyle Lee, Francesco Turro, and Xiaojun Yao, “Quantum Computing for Energy Correlators,” (2024), arXiv:2409.13830 [hep-ph].
- [38] Jack Holguin, Ian Moulton, Aditya Pathak, and Massimiliano Procura, “New paradigm for precision top physics: Weighing the top with energy correlators,” *Phys. Rev. D* **107**, 114002 (2023), arXiv:2201.08393 [hep-ph].
- [39] Jack Holguin, Ian Moulton, Aditya Pathak, Massimiliano Procura, Robert Schöfbeck, and Dennis Schwarz, “Using the W as a Standard Candle to Reach the Top: Calibrating Energy Correlator Based Top Mass Measurements,” (2023), arXiv:2311.02157 [hep-ph].
- [40] Jack Holguin, Ian Moulton, Aditya Pathak, Massimiliano Procura, Robert Schöfbeck, and Dennis Schwarz, “Top Quark Mass Extractions from Energy Correlators: A Feasibility Study,” (2024), arXiv:2407.12900 [hep-ph].
- [41] Patrick T. Komiske, Ian Moulton, Jesse Thaler, and Hua Xing Zhu, “Analyzing N-Point Energy Correlators inside Jets with CMS Open Data,” *Phys. Rev. Lett.* **130**, 051901 (2023), arXiv:2201.07800 [hep-ph].
- [42] Kyle Lee, Aditya Pathak, Iain Stewart, and Zhiqian Sun, “Nonperturbative Effects in Energy Correlators: From Characterizing Confinement Transition to Improving α_s Extraction,” (2024), arXiv:2405.19396 [hep-ph].
- [43] Evan Craft, Kyle Lee, Bianka Meçaj, and Ian Moulton, “Beautiful and Charming Energy Correlators,” (2022), arXiv:2210.09311 [hep-ph].
- [44] Hao-Yu Liu, Xiaohui Liu, Ji-Chen Pan, Feng Yuan, and Hua Xing Zhu, “Nucleon Energy Correlators for the Color Glass Condensate,” *Phys. Rev. Lett.* **130**, 181901 (2023), arXiv:2301.01788 [hep-ph].
- [45] Carlota Andres, Fabio Dominguez, Raghav Kunawalkam Elayavalli, Jack Holguin, Cyrille Marquet, and Ian Moulton, “Resolving the Scales of the Quark-Gluon Plasma with Energy Correlators,” *Phys. Rev. Lett.* **130**, 262301 (2023), arXiv:2209.11236 [hep-ph].
- [46] Carlota Andres, Fabio Dominguez, Jack Holguin, Cyrille Marquet, and Ian Moulton, “A Coherent View of the Quark-Gluon Plasma from Energy Correlators,” (2023), arXiv:2303.03413 [hep-ph].
- [47] João Barata, José Guilherme Milhano, and Andrey V. Sadofyev, “Picturing QCD jets in anisotropic matter: from jet shapes to energy energy correlators,” *Eur. Phys. J. C* **84**, 174 (2024), arXiv:2308.01294 [hep-ph].
- [48] Carlota Andres, Fabio Dominguez, Jack Holguin, Cyrille Marquet, and Ian Moulton, “Seeing Beauty in the Quark-Gluon Plasma with Energy Correlators,” (2023), arXiv:2307.15110 [hep-ph].
- [49] Balbeer Singh and Varun Vaidya, “Factorization for energy-energy correlator in heavy ion collision,” (2024), arXiv:2408.02753 [hep-ph].
- [50] “Energy-energy correlators from PbPb and pp collisions at 5.02 TeV,” (2024).
- [51] Hannah Bossi, Arjun Srinivasan Kudinoor, Ian Moulton, Daniel Pablos, Ananya Rai, and Krishna Rajagopal, “Imaging the Wakes of Jets with Energy-Energy-Energy Correlators,” (2024), arXiv:2407.13818 [hep-ph].
- [52] Yibei Li, Ian Moulton, Solange Schrijnder van Velzen, Wouter J. Waalewijn, and Hua Xing Zhu, “Extending Precision Perturbative QCD with Track Functions,” *Phys. Rev. Lett.* **128**, 182001 (2022), arXiv:2108.01674 [hep-ph].
- [53] Hao Chen, Max Jaarsma, Yibei Li, Ian Moulton, Wouter J. Waalewijn, and Hua Xing Zhu, “Collinear Parton Dynamics Beyond DGLAP,” (2022), arXiv:2210.10061 [hep-ph].
- [54] Hao Chen, Max Jaarsma, Yibei Li, Ian Moulton, Wouter J. Waalewijn, and Hua Xing Zhu, “Multi-Collinear Splitting Kernels for Track Function Evolution,” (2022), arXiv:2210.10058 [hep-ph].
- [55] Max Jaarsma, Yibei Li, Ian Moulton, Wouter J. Waalewijn, and Hua Xing Zhu, “Energy correlators on tracks: resummation and non-perturbative effects,” *JHEP* **12**, 087 (2023), arXiv:2307.15739 [hep-ph].
- [56] Ankita Budhraj and Wouter Waalewijn, “FastEEC 0.3,” (2024), <https://github.com/abudhraj/FastEEC/>

- releases/tag/0.3.
- [57] Samuel Alipour-fard, “ResolvedEnergyCorrelators (RENCs),” <https://github.com/samcaf/ResolvedEnergyCorrelations> (2024).
 - [58] Duff Neill and Felix Ringer, “Soft Fragmentation on the Celestial Sphere,” JHEP **06**, 086 (2020), arXiv:2003.02275 [hep-ph].
 - [59] Lin Dai, Chul Kim, and Adam K. Leibovich, “Large N -point energy correlator in the collinear limit,” (2024), arXiv:2410.11614 [hep-ph].
 - [60] “CERN Open Data Portal,” <http://opendata.cern.ch>.
 - [61] CMS Collaboration, “Jet primary dataset in AOD format from RunA of 2011 (/Jet/Run2011A-12Oct2013-v1/AOD),” CERN Open Data Portal (2016), 10.7483/OPENDATA.CMS.UP77.P6PQ.
 - [62] Patrick T. Komiske, Radha Mastandrea, Eric M. Metodiev, Preksha Naik, and Jesse Thaler, “Exploring the Space of Jets with CMS Open Data,” Phys. Rev. **D101**, 034009 (2019), arXiv:1908.08542 [hep-ph].
 - [63] Patrick Komiske, Radha Mastandrea, Eric Metodiev, Preksha Naik, and Jesse Thaler, “CMS 2011A Open Data || Jet Primary Dataset || $p_T > 375$ GeV || MOD HDF5 Format,” (2019), 10.5281/zenodo.3340205.
 - [64] Daniele Bertolini, Tucker Chan, and Jesse Thaler, “Jet Observables Without Jet Algorithms,” JHEP **04**, 013 (2014), arXiv:1310.7584 [hep-ph].
 - [65] Daniele Bertolini, Jesse Thaler, and Jonathan R. Walsh, “The First Calculation of Fractional Jets,” JHEP **05**, 008 (2015), arXiv:1501.01965 [hep-ph].
 - [66] Kyle Lee, Ian Mould, and Xiaoyuan Zhang, “Revisiting Single Inclusive Jet Production: Timelike Factorization and Reciprocity,” (2024), arXiv:2409.19045 [hep-ph].
 - [67] Jasmine Brewer, José Guilherme Milhano, and Jesse Thaler, “Sorting out quenched jets,” Phys. Rev. Lett. **122**, 222301 (2019), arXiv:1812.05111 [hep-ph].
 - [68] Christian Bierlich *et al.*, “A comprehensive guide to the physics and usage of PYTHIA 8.3,” SciPost Phys. Codeb. **2022**, 8 (2022), arXiv:2203.11601 [hep-ph].
 - [69] Richard Corke and Torbjorn Sjostrand, “Interleaved Parton Showers and Tuning Prospects,” JHEP **03**, 032 (2011), arXiv:1011.1759 [hep-ph].
 - [70] Matteo Cacciari, Gavin P. Salam, and Gregory Soyez, “The anti- k_t jet clustering algorithm,” JHEP **04**, 063 (2008), arXiv:0802.1189 [hep-ph].
 - [71] Patrick T. Komiske, “EnergyEnergyCorrelators package,” <https://github.com/pkomiske/EnergyEnergyCorrelators>.

**SUPPLEMENTAL MATERIAL TO
NEW ANGLES ON ENERGY CORRELATORS**

In this *Supplemental Material*, we provide additional details regarding the parametrization we introduce for projected and resolved N -point energy correlators (PENCs and RENCs, respectively). In App. A, we discuss and visualize the theoretical similarities between our new parametrization and the standard parametrization for PENCs. In App. B, we discuss the algorithmic implementation and the performance of our new parametrization. We also show additional results using Open Data, up to RE4Cs, in App. C, and visualize the process dependence of our PENCs and RENCs on samples for QCD-, W^- , and top-initiated jets in App. D. Finally, in App. E, we discuss the qualitative behavior of non-perturbative effects.

Appendix A: NLL Equivalence to Traditional PENCs

We first emphasize that the parametrization we propose for PENCs only differs from the traditional PENCs studied in the literature through the jet function. In particular, the factorization for our new parametrization is identical to that of the traditional PENCs in the collinear limit [24, 25]:

$$\Sigma_N(R_1, Q) = \int_0^1 dx, x^N \sum_i H_i\left(x, \frac{Q}{\mu}\right) \cdot J_i\left(\frac{x^2 Q^2 R_1^2}{\mu^2}\right), \quad (\text{A1})$$

where the flavor index $i = q, g$ is summed over. At a specific perturbative order, the expressions also depend on μ through $\alpha_s(\mu)$. Eq. (A1) states that the resummed cross section for the PENCs is governed by:

- A *hard function* $H_i(x, Q/\mu)$, characterizing the number density of partons of partonic flavor i (e.g. up quark, gluon) emerging from the hard process at a given momentum fraction x . The hard function is dependent on a renormalization scale μ . Notably, the hard function is independent of the parametrization used for the PENC.
- A *jet function* $J_i(x^2 Q^2 R_1^2/\mu^2)$, describing the subsequent evolution of the energetic parton i into a jet of “final-state” partons on which the PENC is then measured. Unlike the hard function, the jet function depends on the parametrization of the observable.

In this appendix, we quantify the difference between the jet function for our new PENC (the R_1 jet function) and the traditional PENC (the R_L jet function). Using theoretical arguments and numerical evidence, we argue that their difference is only relevant at next-to-next-to-leading-logarithmic (NNLL) order.

The resummation of logarithms of R_1 in Σ_N can be achieved by evaluating the hard function at the scale $\mu_H \sim Q$ and the jet function at the scale $\mu_J \sim QR_1$, and using the renormalization group equations to evolve them to a common scale μ . Since the full PENC is independent of μ , and the hard function is independent of the specific parametrization of the PENC, the renormalization group evolution for the jet function is also parametrization-independent (even if its functional form is not).

Within a jet consisting of two outgoing particles, the PENC we introduce and the traditional PENC are exactly the same, since $R_1 = R_L$. Therefore, the R_1 jet function the R_L jet function are identical at $\mathcal{O}(\alpha_s)$, implying that the cross section for the new and traditional PENC will be equal at NLL, as these are single-logarithmic observables. However, R_1 and R_L will differ for a jet of three particles or more, corresponding to an $\mathcal{O}(\alpha_s^2)$ difference between the R_1 and R_L jet functions, and an NNLL effect in the resummed cross section.

Though R_1 and R_L differ in a generic jet, we note that $R_1 \leq R_L \leq 2R_1$ by the triangle inequality. Therefore, we expect an approximate relationship between the two of the form $R_L \sim (1+c)R_1$ with $0 < c < 1$. Furthermore, NLL equivalence of the R_1 and R_L jet functions implies that $c \sim \mathcal{O}(\alpha_s)$. In particular, writing the N^kLL contribution to the traditional PENC as $\sum_n d_{n,k} \alpha_s^{n+k} \log^n R_L$ and inserting $R_L = (1+c)R_1$ yields:

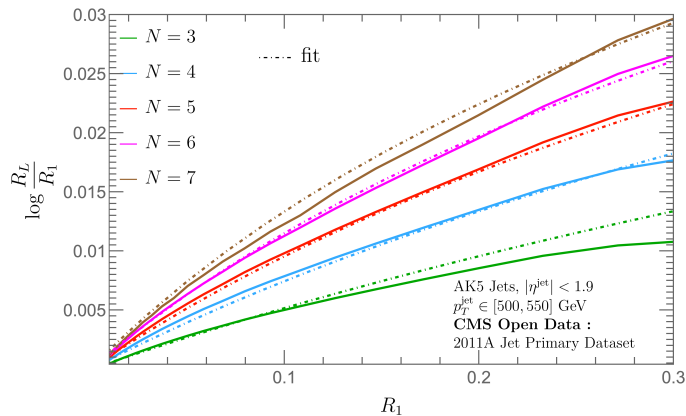


FIG. 5. Difference between the new parametrization (R_1) and the old parametrization (R_L) obtained from corresponding quantiles of the cumulative distributions. The dashed lines correspond to a fit (of the overall coefficient) of the difference $\log(R_L/R_1)$ to $\frac{\alpha_s}{\pi} \log(1 + R_L(N-1))$ for integer values of N from 3 to 7.

$$\begin{aligned}
 \sum_{n,k} d_{n,k} \alpha_s^{n+k} \log^n[R_1(1+c)] &= \sum_{n,k} d_{n,k} \alpha_s^{n+k} [\log R_1 + \log(1+c)]^n \\
 &= \sum_{m,k,k'} \binom{m+k'}{m} d_{m+k',k} \alpha_s^{m+k+k'} \log^m R_1 \log^{k'}(1+c), \quad (\text{A2})
 \end{aligned}$$

where in the final line we have written $n = m + k'$. The terms with $k' = 0$ give precisely the traditional PENC but with the argument R_L replaced by R_1 . For $k' = 1$ this would represent an NLL effect. However, the difference between our new PENC and the traditional PENC starts at NNLL, implying that $\log(1+c) \sim \mathcal{O}(\alpha_s)$ and thus $c \sim \mathcal{O}(\alpha_s)$.

Finally, we present additional numerical evidence that $R_L \sim (1+c)R_1$ with $c \sim \mathcal{O}(\alpha_s)$ by using the cumulative distributions for R_1 and R_L to construct a correspondence between R_1 and R_L using quantiles [67]. In particular, we numerically invert the equation

$$\Sigma_N^{\text{new}}(R_1) = \Sigma_N^{\text{old}}(R_L(R_1)), \quad (\text{A3})$$

to find a functional form for $R_L(R_1)$. In words, Eq. (A3) selects a function $R_L(R_1)$ for which our new PENC and the traditional PENC have equivalent cumulative distributions. Fig. 5 displays the difference between $\log(R_L(R_1))$ and $\log R_1$, as a function of R_1 , for $N = 3, 4, 5, 6$, and 7 . The dashed lines correspond to a fit (of the overall constant) to the form $c \sim \alpha_s/\pi \log[1 + (N-1)R_L]$. This provides numerical evidence for our theoretical arguments that the R_1 and R_L jet functions are equivalent at NLL, and that $R_L = [1 + \mathcal{O}(\alpha_s)]R_1$.

Appendix B: Samples, Implementation, and Performance

The studies of this Letter involve both CMS Open Data jet samples from the CMS 2011A Jet Primary Dataset [60, 61] – also available in MIT Open Data format [62, 63] – and jets in simulated proton-proton collision events generated using `Pythia 8.310` [68] with the default 4C tune [69]. In `Pythia 8.310`, we consider jets initiated by QCD interactions, W bosons, and top quarks, and generate events at hadron level including initial-state radiation, final-state radiation, and multi-parton interactions.

Both the CMS 2011A dataset and our simulated `Pythia` events feature anti- k_t jets [70] with transverse momenta $p_{T,\text{jet}} \in [500, 550]$ GeV and pseudo-rapidity $|\eta^{\text{jet}}| < 1.9$; however, the CMS dataset involves jets of radius $R_{\text{jet}} = 0.5$, while our `Pythia` studies use jets of radius $R_{\text{jet}} = 0.8$, which are more appropriate for capturing the substructure of boosted W -boson- and top-quark-initiated jets. Our samples are summarized in Table I. Finally, we note that all of the traditional PENCs shown in this are calculated with the `EnergyEnergyCorrelators` package [71].

Jet Sample	Center of Mass Energy	AK Radius	
CMS Open Data	7 TeV	$R = 0.5$	
Pythia 8.310			Command in Pythia
QCD Jets	14 TeV	$R = 0.8$	HardQCD:all=on
W Jets	14 TeV	$R = 0.8$	WeakDoubleBoson:ffbar2WW=on
Top Jets	14 TeV	$R = 0.8$	Top:gg2ttbar=on, Top:qqbar2ttbar=on

TABLE I. Jet samples used in this work. All jets have transverse momenta $p_{T,\text{jet}} \in [500, 550]$ GeV and pseudo-rapidity $|\eta^{\text{jet}}| < 1.9$. The color of each row corresponds to the color in the plots of the associated jet sample.

ALG I. Pseudocode for PENC(R_1)

```

1: Output: Normalized 1-dimensional histogram
2:   containing the PENC
3:
4: Initialize 1D histogram to contain the PENC
5: # Loop over jets in a sample:
6: for all  $i$  from 1 to  $n_{\text{jets}}$  do
7:    $jet \leftarrow$  a jet from the desired sample
8:   # Loop over choices for particle  $s$  in the jet:
9:   for all particles  $s$  in  $jet$  do
10:    # Calculate energy weight
11:     $z_s \leftarrow p_{T,s}/(\sum_j p_{T,j})$ 
12:    Sort particles in  $jet$  by angle to  $s$ ,
13:    from smallest to largest
14:    # Prepare to record total weight within a
15:    # distance  $R_1$  of  $s$ , beginning with  $R_1 = 0$ 
16:    Initialize  $sum_{z_1} \leftarrow z_s$ 
17:     $histogram[0] += z_s^N$ 
18:    # Loop over remaining particles  $i_1$ 
19:    for all  $i_1$  from 1 to  $\text{len}(\text{particles})$  do
20:       $R_1 \leftarrow$  angle between  $s$  and  $\text{particle}[i_1]$ 
21:       $z_1 \leftarrow p_{T,i_1}/(\sum_j p_{T,j})$ 
22:      # Calculate contribution to  $d\Sigma$ , and
23:      # update hist. bin for  $R_1$ 
24:       $histogram[R_1] += z_s \times$ 
25:       $((sum_{z_1} + z_1)^{N-1} - sum_{z_1}^{N-1})$ 
26:      # Update sum on weights within  $R_1$ 
27:       $sum_{z_1} += z_1$ 
28:    end for
29:  end for
30: end for
31:
32: # histogram currently contains  $d\Sigma$ , and we want
33: #  $\text{PENC} = d\Sigma/dR_1$ 
34: Process histogram into a probability density by
35:   normalizing it relative to bin widths
36: Write histogram to output file

```

ALG II. Pseudocode for RE3C(R_1, R_2, ϕ_2)

```

1: Output: Normalized 3-dimensional histogram
2:   containing the RE3C
3:
4: Initialize 3D histogram to contain the RE3C
5: # Loop over jets in a sample:
6: for all  $i$  from 1 to  $n_{\text{jets}}$  do
7:    $jet \leftarrow$  a jet from the desired sample
8:   # Loop over choices for particle  $s$  in the jet:
9:   for all particles  $s$  in  $jet$  do
10:    # Calculate energy weight
11:     $z_s \leftarrow p_{T,s}/(\sum_j p_{T,j})$ 
12:    Sort particles in  $jet$  by angle to  $s$ ,
13:    from smallest to largest
14:    # Loop over remaining particles  $i_1$  and  $i_2$ ,
15:    for all  $i_1$  from 1 to  $\text{length}(\text{particles})$  do
16:       $R_1 \leftarrow$  angle between  $s$  and  $\text{particle}[i_1]$ 
17:       $z_1 \leftarrow p_{T,i_1}/(\sum_j p_{T,j})$ 
18:      # where  $i_2$  is closer to  $s$  than  $i_1$ 
19:      for all  $i_2 < i_1$  do
20:         $R_2 \leftarrow$  angle between  $s$  and  $i_2$ 
21:         $z_2 \leftarrow p_{T,i_2}/(\sum_j p_{T,j})$ 
22:         $\phi_2 \leftarrow$  angle associated with  $i_1-s-i_2$ 
23:        # Calculate contribution to  $d\Sigma$ ,
24:        # and update associated hist. bin
25:         $histogram[R_1][R_2][\phi_2] += z_s \cdot z_1 \cdot z_2$ 
26:      end for
27:    end for
28:  end for
29: end for
30:
31: # histogram currently contains  $d\Sigma$ , and we want
32: #  $\text{RE3C} = d\Sigma/dR_1 dR_2 d\phi_2$ 
33: Process histogram into a probability density by
34:   normalizing it relative to bin widths
35: Write histogram to output file

```

We also provide pseudocode of our new algorithms for calculating PENCs and RE3Cs in Algs. I and II, respectively. Alg. I exemplifies how the parametrization we introduce for the PENC (i.e. of angles with respect to a specific particle s) simplifies the N -dependence of our new PENC, and dramatically speeding up the associated computation. In particular, *there are no additional computational complications for large or non-integer N* . For completeness, we also present pseudocode for the RE3C in Alg. II, which features similar computational simplicity and can be easily

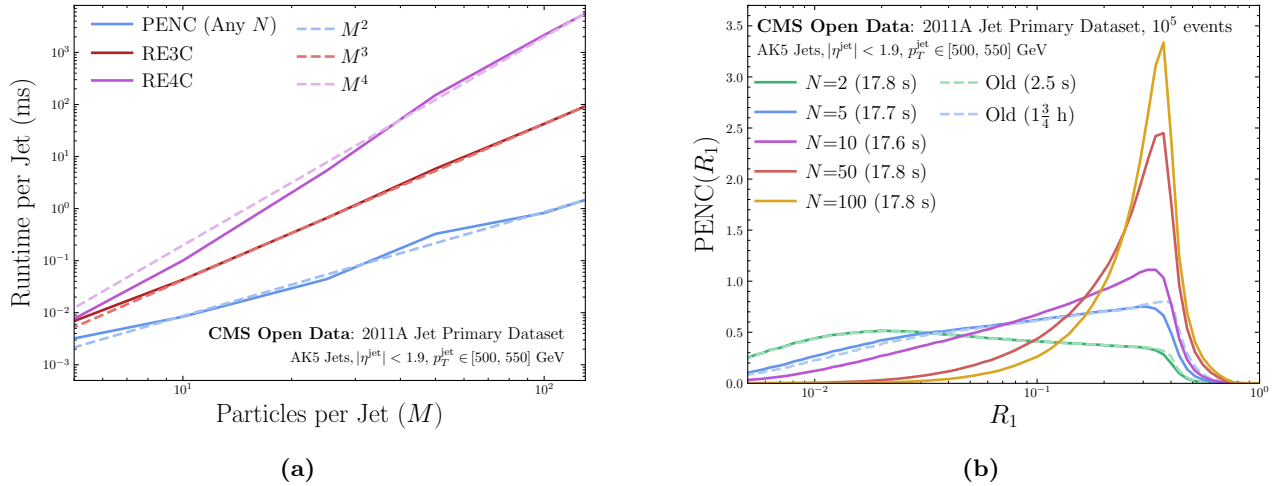


FIG. 6. Plots emphasizing the computational performance of the energy correlators we introduce in this work. **(a)** Runtime of the PENC and RENC code of Ref. [57] on CMS Open Data as a function of the number of particles in a jet, together with a polynomial fit to guide the eye. **(b)** PENCs for $N = 2, 5, 10, 50$, and 100 , each computed using on 10^5 CMS Open Data jets in less than thirty seconds. The solid lines show the PENCs introduced in this work, and the dashed lines show the traditional PENCs. Even for $N = 5$, the traditional computation takes 6266 seconds (close to 2 hours) to run on the same CMS Open Data samples, and the computation time grows exponentially as N increases. The large values of N , which are computationally inaccessible to the traditional PENC even for $N = 10$, are chosen to stress that the PENCs we introduce in this work make quick work of previously unimaginable computations.

generalized to a double-projected ENC as discussed in the main text. For a more complete and technical description of each computation, including permutation factors and contact terms, please consult our implementation available on GitHub at [ResolvedEnergyCorrelators](#) [57].

Finally, in Fig. 6, we display the computational runtime of our code for the evaluation of PENCs and RENCs on jet samples from CMS Open Data. Fig. 6(a) shows how the scaling time for each nearly follows an M^r scaling, where r indicates the number of resolved emissions. Furthermore, the independence of the runtime on the value of N allows us to compute the PENC for enormous, and previously unimaginable, values of N ; some examples up to $N = 100$ are shown in Fig. 6(b). We highlight that our implementation takes similar runtime for all values of N . Therefore, we expect the PENC we introduce in this work to significantly benefit ongoing studies which apply energy correlators in jets produced in heavy-ion collisions for revealing the emergent scales of the quark-gluon plasma in these environments.

Appendix C: Visualizing CMS Open Data with Resolved Correlators

In this appendix, we provide additional polar heat maps, or *bullseye* visualizations, of RE3Cs and RE4Cs evaluated on CMS Open Data, which yield an intuitive view into the internal structure of jets enabled by our new parametrization. We expect that similar visualizations will benefit current and future studies of jet substructure at the LHC.

The bullseyes for the RE3C, shown in Fig. 7, have a radial variable corresponding to the ratio $R_2/R_1 < 1$, with a polar angle corresponding to ϕ_2 . Similarly, the bullseyes for the RE4C in Fig. 8 use the radial variable $R_3/R_2 < 1$ and the corresponding polar variable ϕ_3 . The bullseyes are normalized to a radial measure, such that the bullseye plots provide a faithful representation of each correlator; for the RE3C, the bullseye is normalized to unity against the measure $d \log R_1 \times R_2 dR_2 d\phi_2$, while the bullseyes for the RE4C are normalized to unity against $d \log R_1 d(R_2/R_1) d\phi_2 \times R_3 dR_3 d\phi_3$.

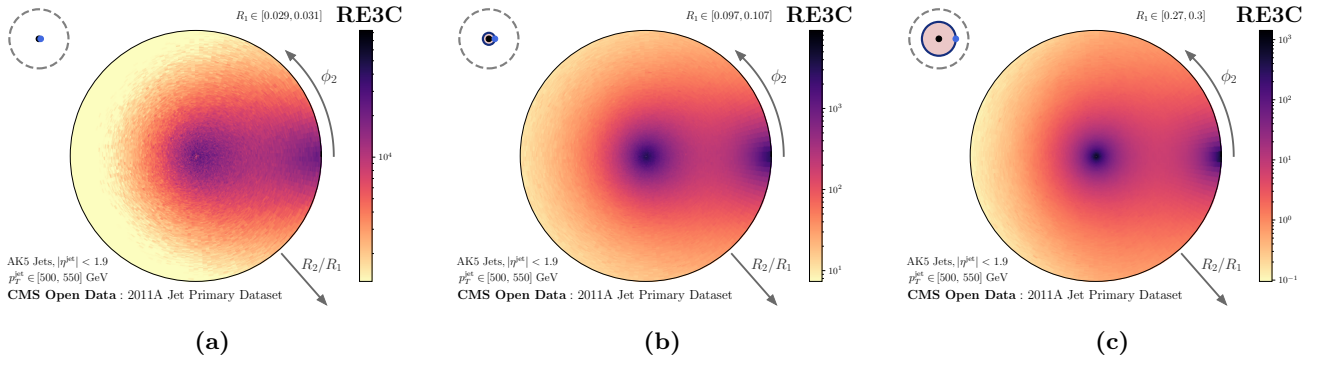


FIG. 7. Additional polar heat maps for RE3Cs evaluated on CMS Open Data. There are enhanced correlations when $R_2 \sim 0$, corresponding to the collinear enhancement as i_2 approaches s , and when $\phi_2 \sim 0$, $R_2 \sim R_1$, corresponding to $i_2 \rightarrow i_1$. The R_1 bin for each plot is indicated by the radius of the filled circle in the top-left inset of each plot.

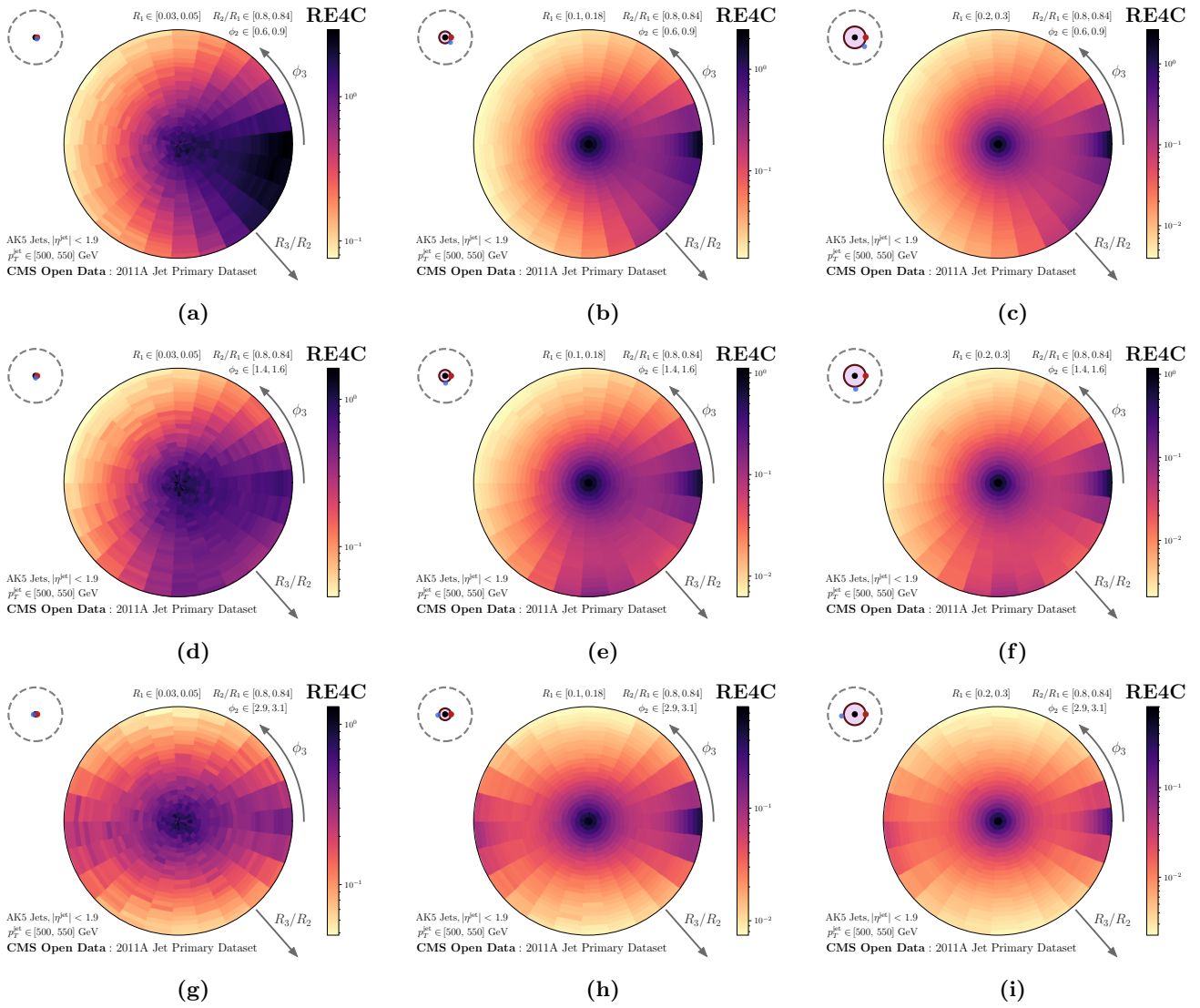


FIG. 8. Polar heat maps for RE4Cs evaluated on CMS Open Data, with ϕ_2 centered near 45° (top row), 90° (middle row) and 180° (bottom row). We highlight that, relative to the RE3C presented in Fig. 7, there are enhanced correlations when $\phi_3 \sim -\phi_2$, corresponding to the collinear enhancement of radiation as i_3 approaches i_1 .

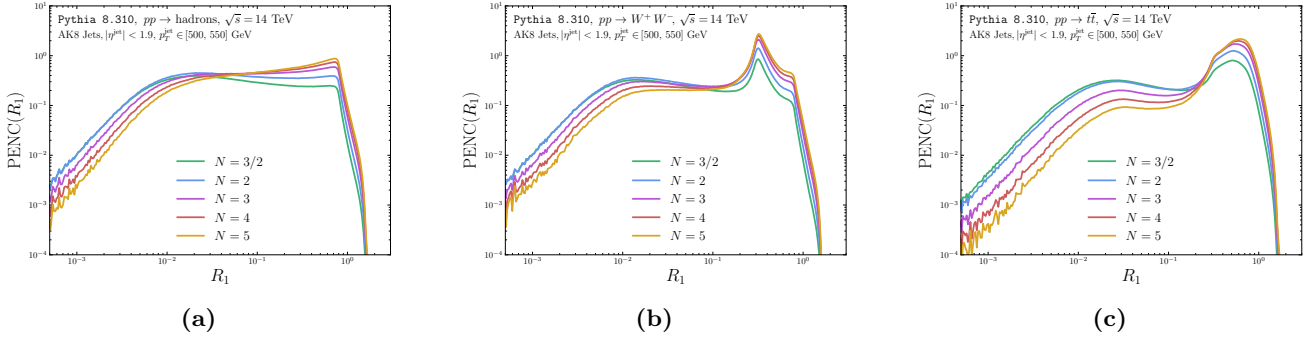


FIG. 9. PENCs for (a) QCD-, (b) W - and (c) top-quark-initiated jet samples generated with `Pythia 8.310`. Jets are clustered using the anti- k_t algorithm with a radius parameter of $R = 0.8$, and have transverse momenta in the range $p_T^{\text{jet}} \in [500, 550]$ GeV and pseudo-rapidities in the range $|\eta^{\text{jet}}| < 1.9$. PENCs for W - and top-quark-initiated jets feature enhanced correlations at scales correlated with the W -boson and top-quark masses.

RE3Cs are shown in Fig. 7 for several R_1 bins, and RE4Cs are shown in Fig. 8 for several R_1 and ϕ_2 bins with a fixed R_2/R_1 bin. We note that the RE3C distributions are quite similar across different R_1 bins. On the other hand, for R_2 near R_1 , the RE4C distributions exhibit distinct patterns of radiation depending on the value of ϕ_2 . In particular, Fig. 8 prominently visualizes the collinearly enhanced correlations in the RE4C when ϕ_3 is near $-\phi_2$ and R_3 is near R_1 , i.e. when particle i_3 approaches particle i_1 . For small R_2 , these correlations diminish, and the bullseye visualizations for the RE4C look very similar to that of the RE3C, reflecting the near-scale-invariance of QCD.

Appendix D: Process Dependence: Pythia Samples

This appendix provides visualizations for energy correlators evaluated on Monte Carlo samples of QCD-, W -, and top-initiated jets generated in `Pythia 8.310`, as detailed in Table I, which emphasize both the broad range of applications and the visually intuitive representations of jet substructure that are achieved by our new parametrization for RE3Cs. We begin by showing PENCs evaluated on each jet sample in Fig. 9, which provide simple, albeit less fetching, visualizations which clearly distinguish each sample of jets.

The visually distinct features of each jet sample are even more evident as more particles are resolved, i.e. by the RE3C and RE4C. In Fig. 10, we present bullseye visualizations of the RE3C for each jet sample in several R_1 bins; as in the plots using CMS Open Data in the previous appendix, the radial variable and polar angle for each RE3C bullseye are the ratio R_2/R_1 and the angle ϕ_2 , respectively. We note that the rings in the polar heat maps for the RE3C are correlated with the mass of the W boson, in that they appear at the angular scale $R_2 \simeq 0.3 \sim 2m_W/p_T^{\text{jet}}$.

The bullseye of representation of the RE3C we introduce are similar to the analogous bullseye representations of the traditional E3C for each jet sample, shown in Fig. 11, for which the radial variable is the ratio R_S/R_L and the polar angle is the associated azimuthal angle. However, the traditional E3C shows only a small slice of the information of the RE3C we introduce in this work, and the RE3C introduced in this work contains additional information about the relative orientations of particles within a jet; for example, Figs. 10(h) and 10(k) can be compared to Figs. 11(h) and 11(k) to conclude that the RE3C we introduce conveys additional information about the orientation of the rings of radiation within W -boson-initiated jets.

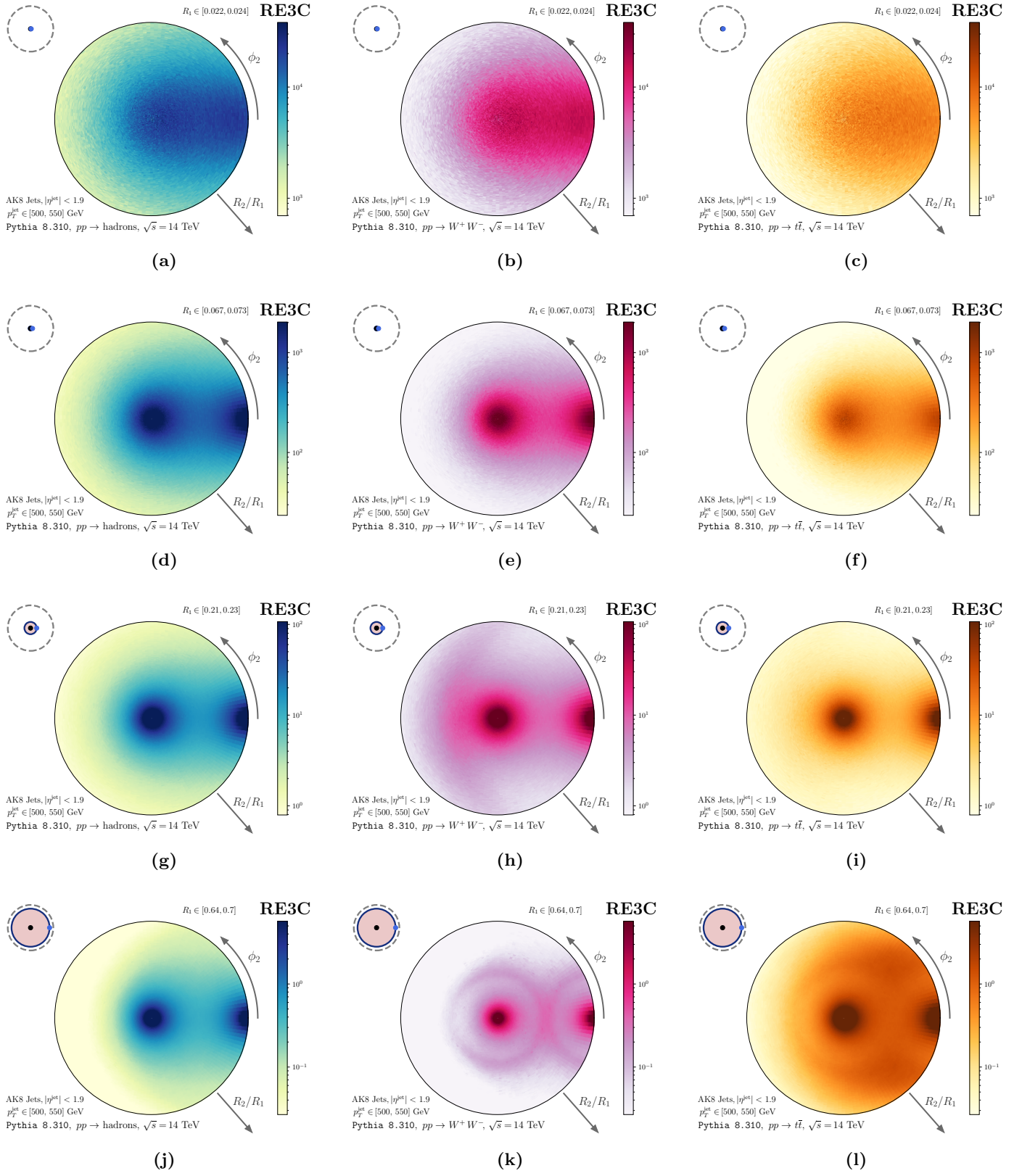


FIG. 10. Polar heat maps of the RE3C we introduce in this work for (first column) QCD-, (second column) W -, and (third column) top-quark-initiated jets. The radial direction in each plot is the ratio R_1/R_2 , and the polar angle of each plot indicates the angle ϕ_2 . Our RE3Cs provide a clear visual representation of the distinct patterns of radiation in each jet sample at different scales (set by R_1).

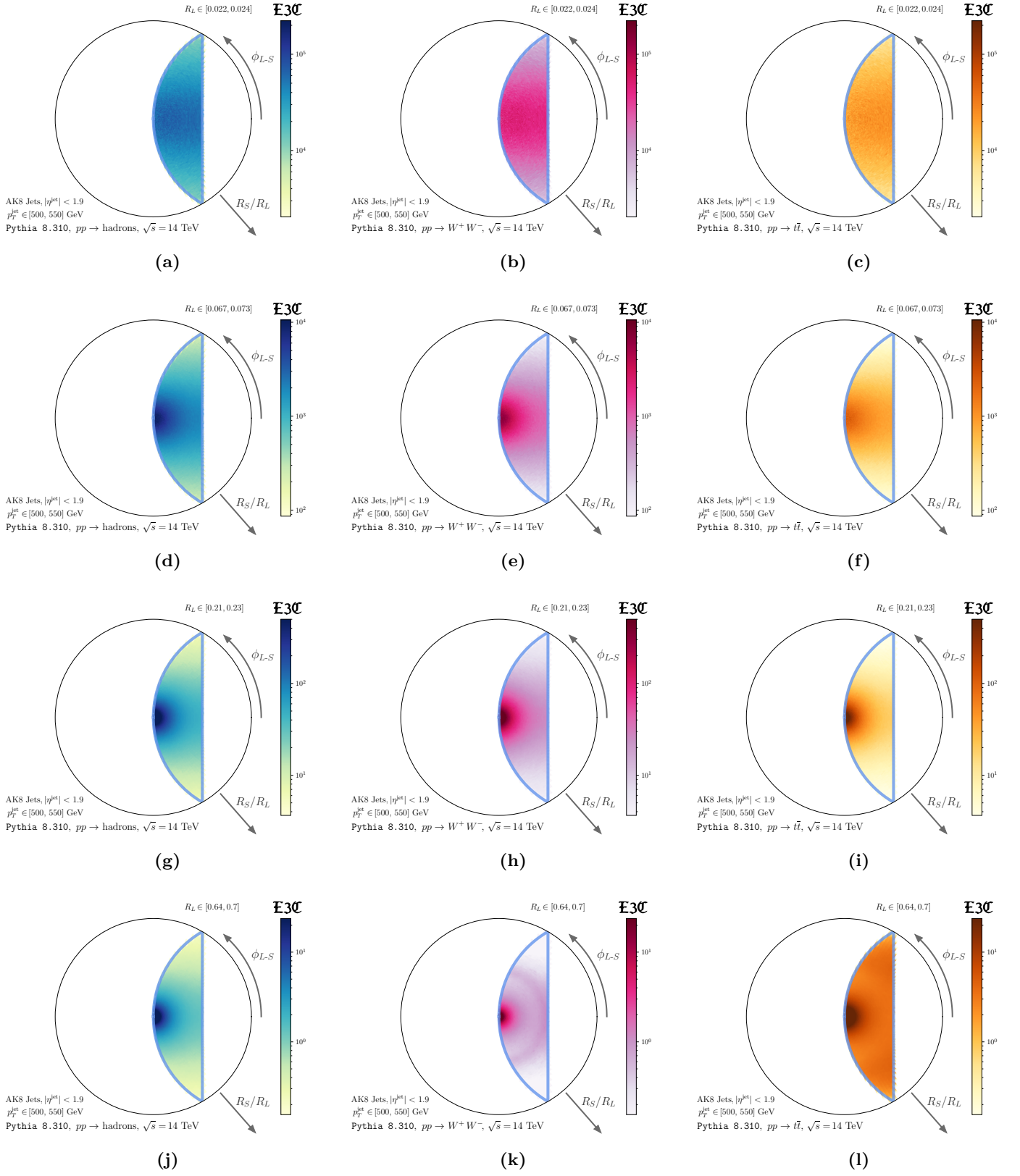


FIG. 11. Polar heat maps of the traditional E3C for (first column) QCD-, (second column) W^- , and (third column) top-quark-initiated jets. The radial direction in each plot is the ratio R_S/R_L , and the polar angle of the plot corresponds to the angle between the lines whose lengths determine R_S and R_L . The R_L bins for each plot are chosen to be the same as the R_L bins in Fig. 10. The polar heat maps of the traditional E3C contain similar information as the RE3Cs introduced in this work and shown in Fig. 10; however, the traditional E3C does not capture all the orientation information about radiation patterns in each jet sample that is present in our new RE3C.

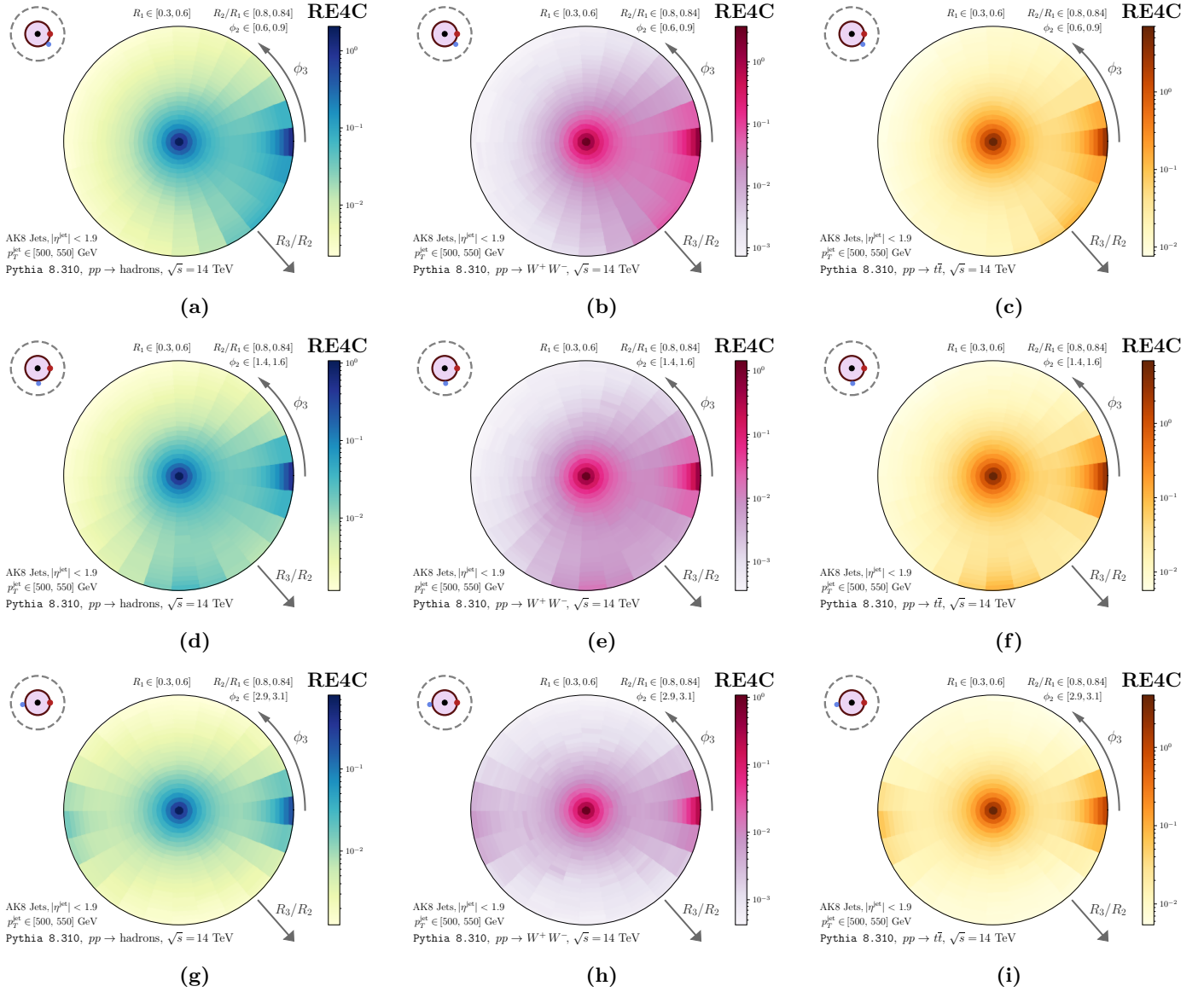


FIG. 12. Bullseye visualizations of the RE4C evaluated on QCD-, W -, and top-quark-initiated jets generated with Pythia 8.310, in the style of Fig. 8. As in Fig. 8, there are also enhanced correlations in energy when ϕ_3 is near $-\phi_2$.

Fig. 12 provides similar polar heat maps for R_3/R_2 and ϕ_3 for the RE4C, within several ϕ_2 bins, and for R_2 near R_1 . As in the case of the RE4Cs evaluated on CMS Open Data, we also see prominent correlations when $\phi_3 \sim -\phi_2$ when R_2 is near R_1 , corresponding to the case that particle i_3 approaches particle i_1 . These correlations for $\phi_3 \sim -\phi_2$ quickly diminish as R_2 is decreased and no longer near R_1 .

Finally, we visualize the ϕ_2 -integrated RE3Cs for each jet sample in the first row of Fig. 13 and the R_M -integrated traditional E3Cs in the second row. Much as in the case of the polar heat maps, the integrated RE3Cs densities provide strictly more information than the densities associated with traditional E3Cs. These provide a clear visual distinction between each sample of jets.

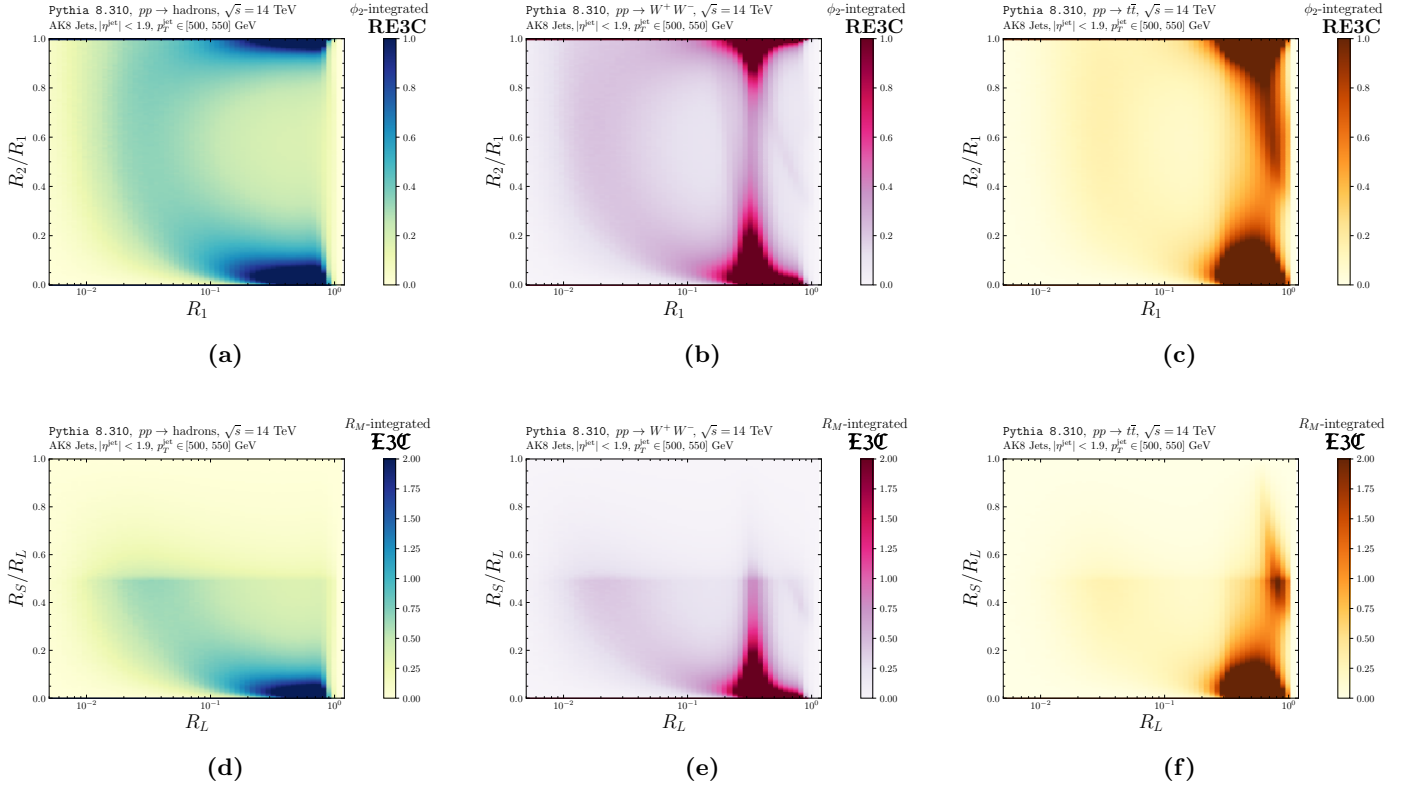


FIG. 13. Density plots for ϕ_2 -integrated RE3Cs (first row) and the analogous R_M -integrated traditional E3Cs (second row), in the style of Fig. 4 of the main text, evaluated on simulated events in `Pythia 8.310`. The first column shows ϕ_2 -integrated RE3Cs for $pp \rightarrow \text{hadrons}$, the second column for $pp \rightarrow W^+W^-$, and the third column for $pp \rightarrow t\bar{t}$. Each row illuminates how three-point energy correlators encode the unique features of each type of jet. We note that the information of the traditional E3C is a subset of the information conveyed by the RE3C we introduce in this work.

Appendix E: Non-Perturbative Features

Finally, we investigate the non-perturbative features of the new RENCs we introduce in this work, focusing on the example provided by the density plots for the ϕ_2 -integrated RE3C which we visualize again in Fig. 14. For notational convenience in the discussion below, we let p_T be shorthand for p_T^{jet} . Unlike in the traditional E3C, for which there are only non-perturbative effects in the squeezed configuration with $R_S \sim \Lambda_{\text{QCD}}/p_T$, our new RE3C exhibits non-perturbative features in two regimes: (1) when $R_2 \sim \Lambda_{\text{QCD}}/p_T$, when particle i_2 (the emission that sets R_2) approaches the special particle s ; and (2) when $R_1 - R_2 \sim \Lambda_{\text{QCD}}/p_T$, with the possibility that i_2 approaches i_1 .

However, the shapes of the non-perturbative features of the integrated RE3C of Fig. 14(a) are not exactly symmetric under a reflection about the line $R_2 = R_1/2$: the ridge in Fig. 14(a) when $R_2 \rightarrow R_1$ has a smaller slope than the ridge when $R_2 \rightarrow 0$. Concretely, this means that R_2 must get closer to R_1 in order for non-perturbative features to emerge than we might naively expect. We refer to this as the “ R_2 -asymmetry” of the integrated RE3C.

To explain this R_2 -asymmetry, we note that when $R_2 \sim \Lambda_{\text{QCD}}/p_T$, shown by the dashed yellow line in Fig. 14, the particle i_2 is non-perturbatively close to s , independent of the orientation ϕ_2 of particle i_2 around s . On the other hand, when $R_2 \sim R_1 - \Lambda_{\text{QCD}}/p_T$, particle i_2 is not guaranteed to be near i_1 . Instead, i_2 is only non-perturbatively close to i_1 in a narrow range of azimuthal angles centered around $\phi_2 = 0$, as visualized in Fig. 14(b). Therefore, it is only when R_2 gets significantly closer to R_1 that the non-perturbative features of the integrated RE3C begin to emerge.

We estimate the R_2 -asymmetry of the integrated RE3C by noting that non-perturbative features emerge when the measure of the non-perturbative phase space for i_2 near i_1 is comparable to the non-perturbative phase space for i_2 near s . This is visualized in Fig. 14(b): non-perturbative features of the integrated RE3C emerge when the length of the green dashed line near i_1 has a length of order Λ_{QCD}/p_T . The associated geometric constraint is a

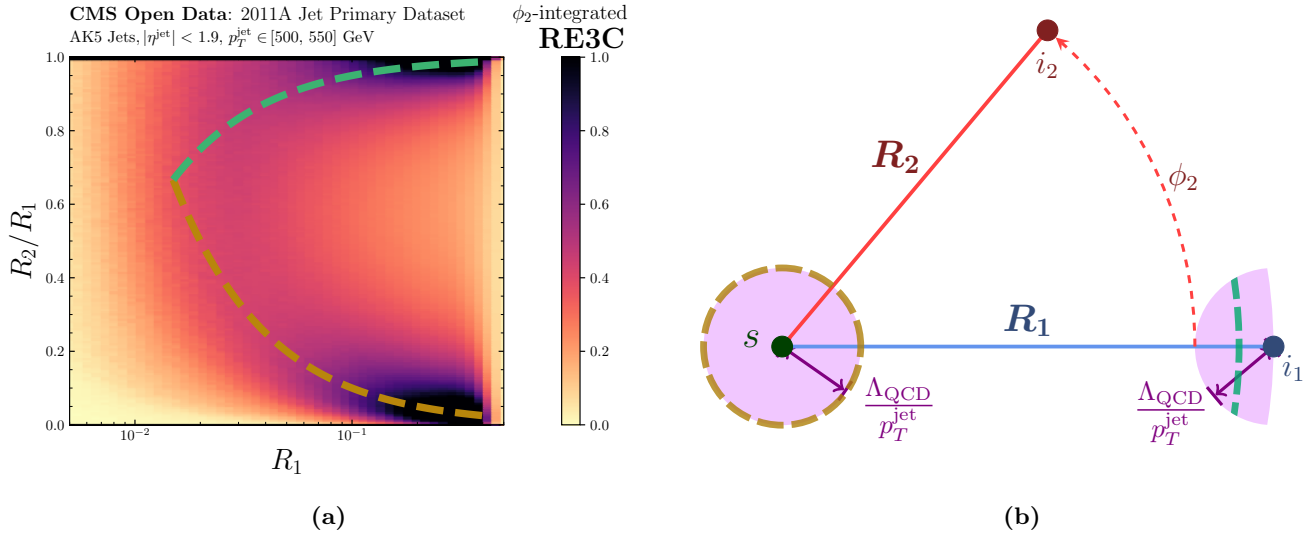


FIG. 14. Depictions of the non-perturbative features of the RE3C introduced in this work **(a)** highlighted in a two-dimensional density plot, and **(b)** in a simple cartoon demonstrating the relevant non-perturbative regimes. **(a)** A density plot for the RE3C evaluated on CMS Open Data and integrated over ϕ_2 , taken from Fig. 4 of the main text, together with dashed lines indicating where non-perturbative effects are expected to become important using (geometric) phase space considerations. **(b)** The RE3C geometry, with non-perturbative regions of phase space highlighted in purple, and with the dashed lines near s and i_2 indicating the values of R_2 where we expect non-perturbative features to emerge in the integrated RE3C.

complicated solution to a cubic equation and we do not show it here. However, we show our resulting estimate of the non-perturbative features as the green dashed line in Fig. 14(a), which aligns closely with the non-perturbative ridge of the integrated RE3C as R_2 approaches R_1 .